Article

Experimental Study on the Spatial−Temporal Failure Characteristics of Red Sandstone with a Cemented Structural Surface under Compression

Ansen Gao,*,[⊥] Chengzhi Qi,*,[⊥] Renliang Shan, and Chunlai Wang

Read Online

ACCESS | Metrics & More | Article Recommendations

AE Precursor of Rock Failure | Spatial-temporal Distribution of Fracture Types of Rocks
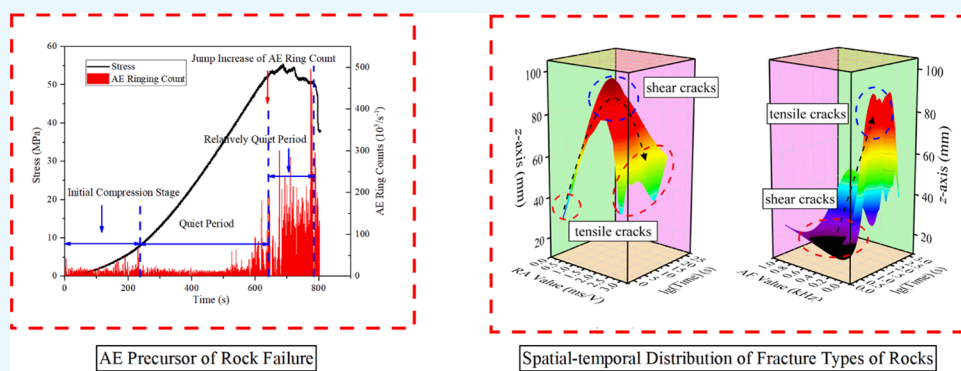
ABSTRACT: A geological structural surface frequently appears in underground engineering and it significantly affects the stability of engineering structures. To elucidate the spatial−temporal failure characteristics of discontinuities between rocks, red sandstone with a firmly cemented discontinuity was investigated under uniaxial compression. The results revealed that adding a strong binder to rock discontinuities can improve the shear strength and stability of rock mass. The stress curve indicated that red sandstone specimens had elastic−brittle failure characteristics without obvious plastic deformation. The acoustic emission ring counts did not have large fluctuations, and its values were smaller (less than 2.5×10^4/s) at elastic deformation stage, which was termed as the "quiet period". The acoustic emission ring counts initially exhibited an obvious jump increase phenomenon at the forthcoming brittle failure stage before stress curve produced an obvious turning point, and then, it entered the "relatively quiet period". Based on the acoustic emission index (rise angle and average frequency), at the initial destruction stage of rocks, the types of internal fractures were simple and clearly (tensile cracks or shear cracks), and the fracture location was also relatively scattered inside specimens. Subsequently, the internal fracture developed into mixed tensile and shear cracks, and then, the fracture location exhibited a progressive evolution trend in the vertical space of specimens.

1. INTRODUCTION

With the needs of social development, various major projects, such as the Sichuan−Tibet Railway, have to be carried out in complex geological areas. This underground engineering, in the tectonic active region, faces severe challenges, such as strong stress disturbance, frequent dynamic disasters, and complex geological structures.[1−3] Hence, it is necessary to clearly evaluate the damage state of engineering rocks for closely monitoring dynamic disasters, such as fault-slip rockburst, when the engineering constructions passing through geological regions.[4−6] Therefore, it is an urgent scientific problem for safely crossing underground faults and geological structural areas.[7]

Tunneling is often associated with fault and geological structural planes and it may affect the stability of tunnels.[8,9] Moreover, many studies have conducted beneficial investiga-

tions on the failure characteristic of rocks with structural planes.[10−17] It had been discovered that mine shocks were related to several corresponding shear fractures in gold mines of South Africa.[10,11] Additionally, it had also been found that the structural plane was fully related to the occurrence of rockburst at Jinping II Hydropower Station.[12,13] However, the fracture evolution pattern and the mechanical characteristics of fault-slip rockburst had not been clearly analyzed by the above-mentioned studies.[8−13] Therefore, we learn that the strength of geological
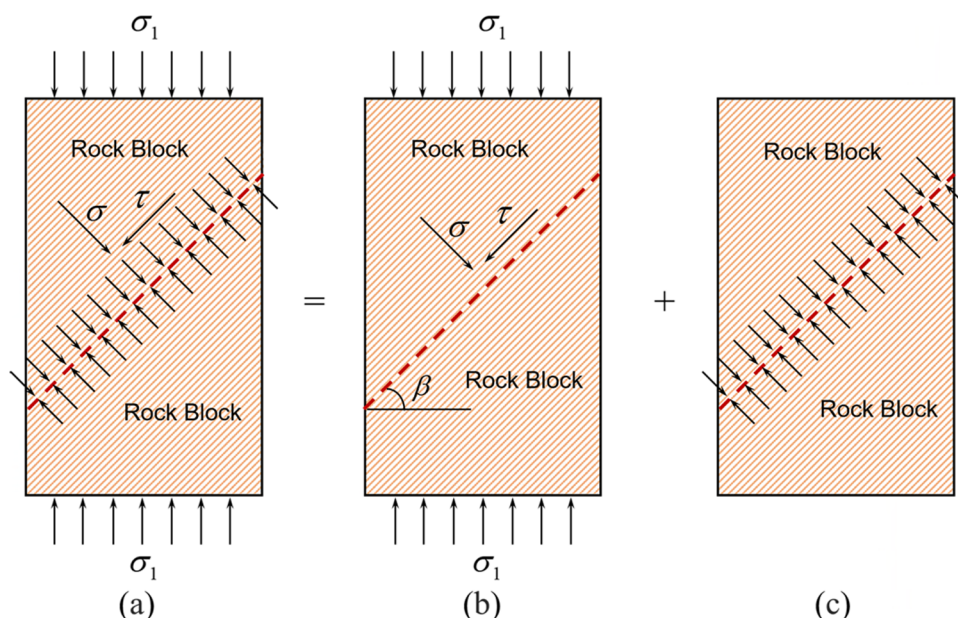
Figure 1. Stress field decomposition of the strongly cemented structural plane: (a) superimposed stress field by original stress and strong cementation force, (b) stress field of original stress, and (c) stress field of strong cementation force.

structural plane will influence the safety of underground engineering. In fact, the weak structural plane has a great impact on the slope, and the body usually slide along the weak structural plane under compression.[14] Still, the damage characteristics of sliding body had not been clearly considered by Song et al.[14] The tunnel rockburst, induced by structural planes, revealed that the progressive slabbing failure may easily activate the internal structural planes and the fault-slip rockburst was more likely to be triggered.[12] However, the mechanical responses of fault-slip rockburst were not adequately elucidated by the above-mentioned studies.[12,14] The structural planes can change the local stress state of rocks and lead to high stress concentration.[13] As the tectonic stress increased, the shear fractures will increase and a crushed area will be gradually formed. However, the types of failure cracks inside rocks were also ignored by Ma et al.[15] Then, the shear failure of joints filled with a cement grout was investigated by Lu et al.[16] However, the fracture type and location within rock specimens were not further analyzed by Lu et al.[16] Zhou et al.[6] reported that the strength of structural planes determined the grade of fault-slip rockburst. Correspondingly, it had been concluded that the structural plane with an angle of 60° can control the stability of rocks.[17] However, its applicability had not been further investigated by the above-mentioned studies.[16,17] Zong et al.[18] found that the shear strength of structural planes was significantly improved by grouting reinforcement. Moreover, the previous shear history can reduce the risk of rockburst.[4−6] Although the water intrusion had a great influence on the support performance of cemented paste,[19−22] the cemented structural surface was insensitive to the influence of water in this study. Therefore, improving the cementation strength of rock discontinuities is one of the main approaches to remedy rock discontinuity defects and improve the stability of rocks.

Consequently, the slip and shear failure along rock discontinuities is one of the main failure modes in underground engineering. Based on this engineering background, this study carried out testing on rock specimens with a strong cemented structural plane under uniaxial compression. The temporal and spatial failure characteristics of rock specimens with strongly cemented discontinuities were analyzed. Moreover, the mechanical response characteristics of strongly cemented structural planes to enhance the stability of rock mass were also revealed. In addition, several suggestions for supporting and controling weak broken rock mass were also analyzed in this study. The results of this study are expected to provide useful insights with regard to the stability controlling of engineering structures with discontinuities.

2. THEORETICAL BASIS

2.1. The Mechanical Model of Shear Failure for Rocks with a Cemented Structural Surface. The test results demonstrated that the maximum compression strength of red sandstone specimens was less than 60 MPa, and the failure strength of strong solid glue was typically greater than 60 MPa. Therefore, it was defined as a strongly cemented structural plane, which was generally greater than the natural strength of original joint plane. In fact, the shear strength of discontinuities is an important factor for describing the mechanical properties of rock mass. For rocks with strongly cemented structural planes, the following situations can be distinguished. If $\tau_s \ll \tau_r$ (τ_s represents the shear failure strength of structural plane and τ_r represents the shear failure strength of rocks), the cracks initiation and fracture propagation developed from the structural plane. If $\tau_s \gg \tau_r$, the fracture location will start from the inner part of rocks.

Assuming that rock blocks slide along the potential structural plane, as shown in Figure 1, both rock blocks and cemented structural plane obey the Mohr−Coulomb failure criterion,[23−25] and the composite rock specimen is anisotropically homogeneous. Then, the following relationship can be obtained.

$$\tau = c + \sigma \tan \varphi \tag{1}$$

where τ is the shear stress of potential structural plane, c and φ are the cohesion and friction angle, respectively, and among them, $c = c_c,\ c_n$ and $\varphi = \varphi_c,\ \varphi_n$. The subscript c indicates the

addition of a reinforcing agent, and the subscript n indicates the absence of a reinforcing agent.

According to the Mohr's stress circle, when a reinforcing agent is not added, the normal stress (σ) and shear stress (τ) of potential sliding structural plane are expressed as follows

$$\sigma = \frac{1}{2}(\sigma_1 + \sigma_3) + \frac{1}{2}(\sigma_1 - \sigma_3)\cos 2\beta \tag{2}$$

$$\tau = \frac{1}{2}(\sigma_1 - \sigma_3)\sin 2\beta \tag{3}$$

where σ_1 is the maximum principal stress (axial stress), σ_1 is the minimum principal stress (confining pressure), and β is the angle between the potential sliding structural plane and the horizontal plane.

Then, from eqs 1–3, the following expression can be obtained

$$\sigma_1 = \sigma_3 + \frac{2(c_n + \sigma_3 \tan \varphi_n)}{(1 - \tan \varphi_n \cot \beta)\sin 2\beta} \tag{4}$$

It has shown that the shear strength of natural potential sliding structural plane is lower when a reinforcing agent is not added.[16,18] After strengthening, the normal stress increment (σ_a) and shear stress increment (τ_a) of cemented structural planes are expressed as follows

$$\sigma_a = \lambda\sigma_1 \cos \theta \tag{5}$$

$$\tau_a = \gamma\sigma_1 \sin \theta \tag{6}$$

where λ and γ are the bond force coefficients which related to the bond strength of rocks.

For strongly cemented structural planes, the following relationships can hold

$$\sigma = \frac{1}{2}(\sigma_1 + \sigma_3) + \frac{1}{2}(\sigma_1 - \sigma_3)\cos 2\beta + \lambda\sigma_1 \cos \theta \tag{7}$$

$$\tau = \frac{1}{2}(\sigma_1 - \sigma_3)\sin 2\beta + \gamma\sigma_1 \sin \theta \tag{8}$$

Then, from eq 1, the following equation can be obtained

$$\sigma_1 = \sigma_3 + \frac{2(c_n + \sigma_3 \tan \varphi_n)}{(1 - \tan \varphi_n \cot \beta)\sin(2\beta)} + \frac{2\lambda\sigma_1 \cos \theta}{(1 - \tan \varphi_n \cot \beta)\sin(2\beta)} \tag{9}$$

Therefore, for the potential sliding structural plane, the shear strength (τ) and the strengthening increment ($\Delta\sigma$) of the strong cementation effect are expressed, respectively, as follows

$$\tau = c_n + \sigma \tan \varphi_n + \lambda\sigma_1 \cos \theta \tag{10}$$

$$\Delta\sigma = \frac{2\lambda\sigma_1 \cos \theta}{(1 - \tan \varphi_n \cot \beta)\sin(2\beta)} \tag{11}$$

2.2. The Method for Distinguishing the Failure Types of Rocks. Acoustic emission (AE) monitoring can reflect the internal failure state of rocks through an elastic wave which released by rock deformation. The location information of rupture source can be monitored by AE technology. However, owing to the limitation of AE monitoring technology, the rupture types of the fracture source for rocks cannot be directly distinguished. Then, the rise angle (RA) and average frequency (AF) of AE wave can be used to distinguish the tensile and shear

fracture types inside rocks,[26−30] as shown in Figure 6 (line 0). In the typical crack classification method by RA value and AF value, the results refer to tensile cracks in the upper area of line 0 in Figure 6, and it refers to shear/mixed-mode cracks in the lower area of line 0 in Figure 6.

Then, the tensile and shear fractures were further clearly distinguished, as shown in Figure 6. The distinguished principle was refined and classified based on the maximum boundary of RA value and AF value. Moreover, the physical meaning of RA value and AF value was also adopted in this study (classification basis of region II). The projected value of RA value was relatively less than 0.3 in AF axis when the tensile fracture occurred inside specimens, while the projected value of RA value was relatively less than 0.3 when the shear fracture occurred. This study visualized the spatial and temporal distribution of rock fracture based on RA and AF values. The calculation formulae were expressed as follows

$$\text{RA} = RT/A \tag{12}$$

$$\text{AF} = C/D \tag{13}$$

where RT represents the rise time of AE wave, A represents the maximum amplitude of AE wave, C represents the AE ring counts, and D is the duration of AE wave, and the physical meaning of AE parameters is shown in Figure 2.
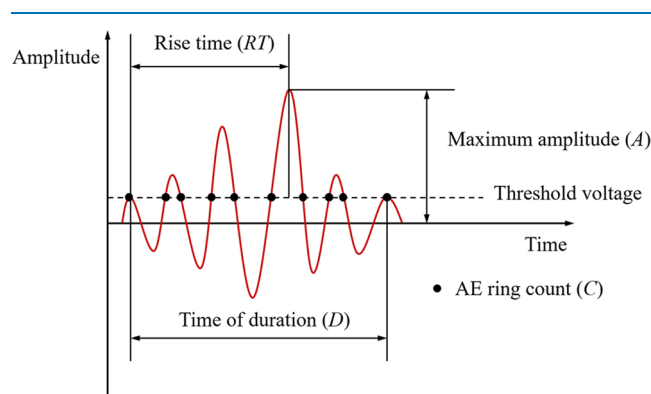

Figure 2. Physical meaning of acoustic emission parameters.

3. EXPERIMENTAL SECTION

3.1. Experimental Equipment. The Instron 5985 compression testing machine (Instron, Buckinghamshire, UK) was used in this study, which had a maximum load capacity of 250 kN, a minimum loading rate of 0.0001 mm/min, and a maximum loading rate of 508 mm/min, as shown in Figure 3a. The AE monitoring equipment employed PCI-II (PAC, State of New Jersey), which was an AE signals acquisition and analysis system, as shown in Figure 3b. To improve the spatial positioning accuracy of AE events, six AE sensors were used in this test, and AE sensors were placed 20 mm away from both ends of rock specimens, as shown in Figure 3c. In addition, AE sensors were distributed at an angle of 90° to ensure that all AE sensors were not coplanar. The threshold value of AE monitoring system was set to 45 dB, the preamplifier gain was set to 40 dB, and the sampling frequency was set to 1 MHz.

3.2. Sample Preparation. The same raw rock sample was used for specimens preparation to ensure that the bedding structure and the physical and mechanical parameters of specimens had the same level of magnitude. According to ISRM (International Society for Rock Mechanics) suggested
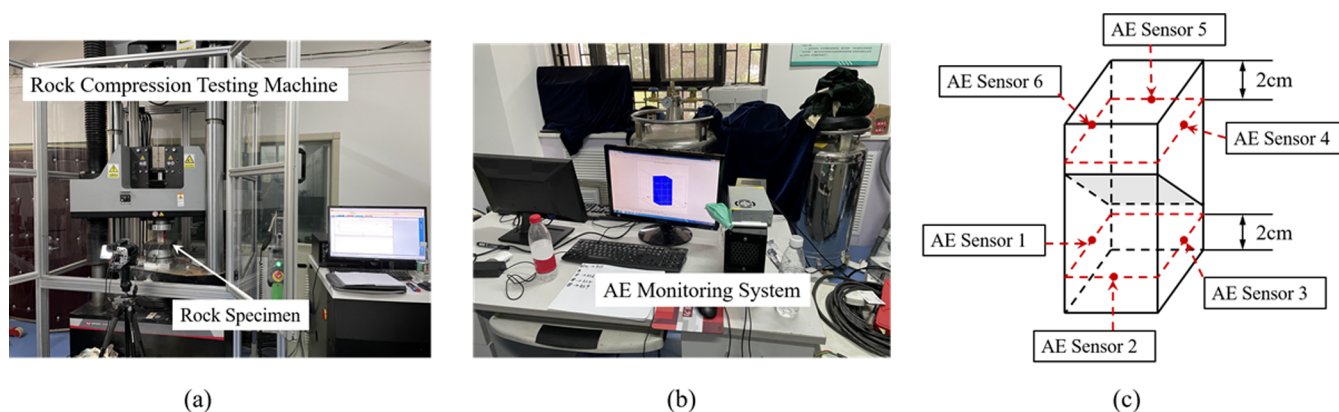
Figure 3. Experimental equipment: (a) compression testing machine, (b) AE monitoring equipment, and (c) location distribution of AE sensors.

method, the specimens were prepared as square cubes with a height−diameter ratio of 2:1 and a size of $50 \times 50 \times 100$ mm^3. After preliminary preparation, the specimens were carefully polished to ensure that both ends were ground flat without significant damage. The nonparallelism of specimens end face was less than 0.05 mm and the axial deviation was less than 0.25°, as shown in Figure 4. Subsequently, the rock specimen

Figure 4. Part of rock specimens after processing.

was cut into two parts with equal size, and the angle between the cutting direction and horizontal direction was 45°. Then, the specimens were glued together using strong solid glue, and to ensure the thickness of bond was same as the thickness of slit. When the bonded specimen was essentially fixed, the excess burr and uneven bonding were removed. Then, six red sandstone specimens with strong cemented structural planes were prepared for this test, and the representative specimens B5 and B6 were selected for analyzing the failure characteristics of rocks with cemented structural surfaces.

3.3. Experimental Method. The loading rate was set to 0.2 mm/min to ensure that the loading rate was within static load range $(10^{-5}-10^{-1}/\text{s})$. The loading process was monitored synchronously with AE monitoring. Beyond the peak stress of red sandstone specimens, the loading process will be stopped after the stress dropped to 80% of its peak value to ensure specimens had been completely destroyed. Then, the AE monitoring information was obtained, and the AE event localization was also conducted by the localization algorithm.[31]

4. RESULTS

4.1. Microscopic Failure Characteristics of Rocks with Strongly Cemented Discontinuities. As shown in Figure 5, the AE ring counts are relatively calm (its value is less than 2.5 ×
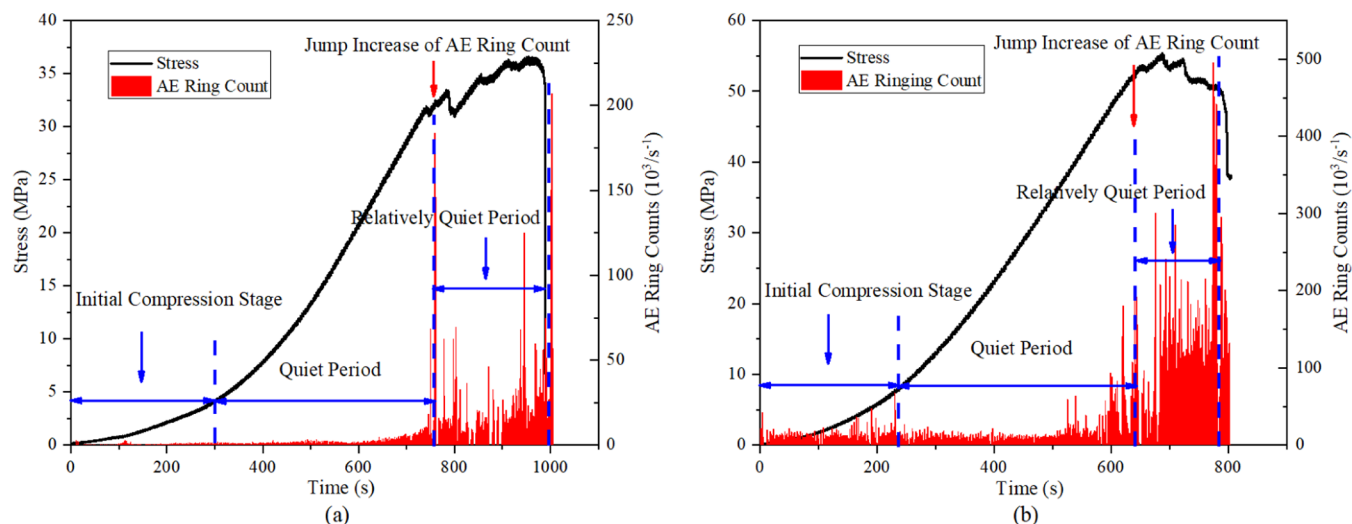

Figure 5. Typical AE precursor characteristics of red sandstone failure under compression: (a) AE ring counts of specimen B5 and (b) AE ring counts of specimen B6.
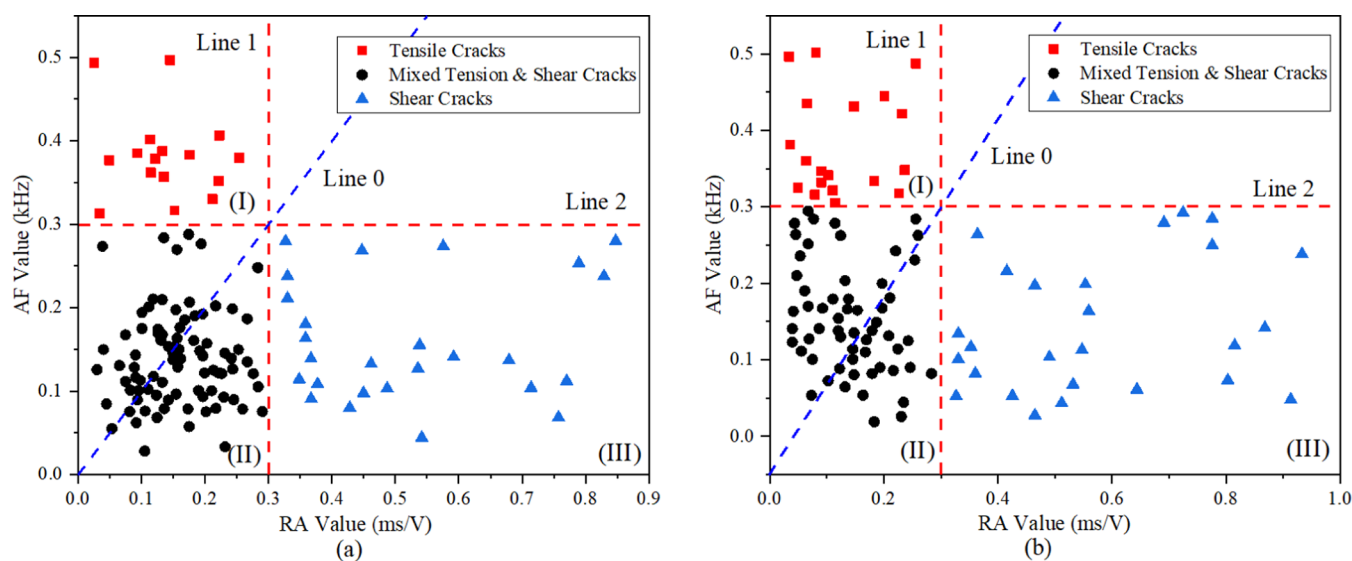
Figure 6. Failure type definition of the red sandstone specimens by AF and RA values under compression: (a) AF and RA values of specimen B5 and (b) AF and RA values of specimen B6.
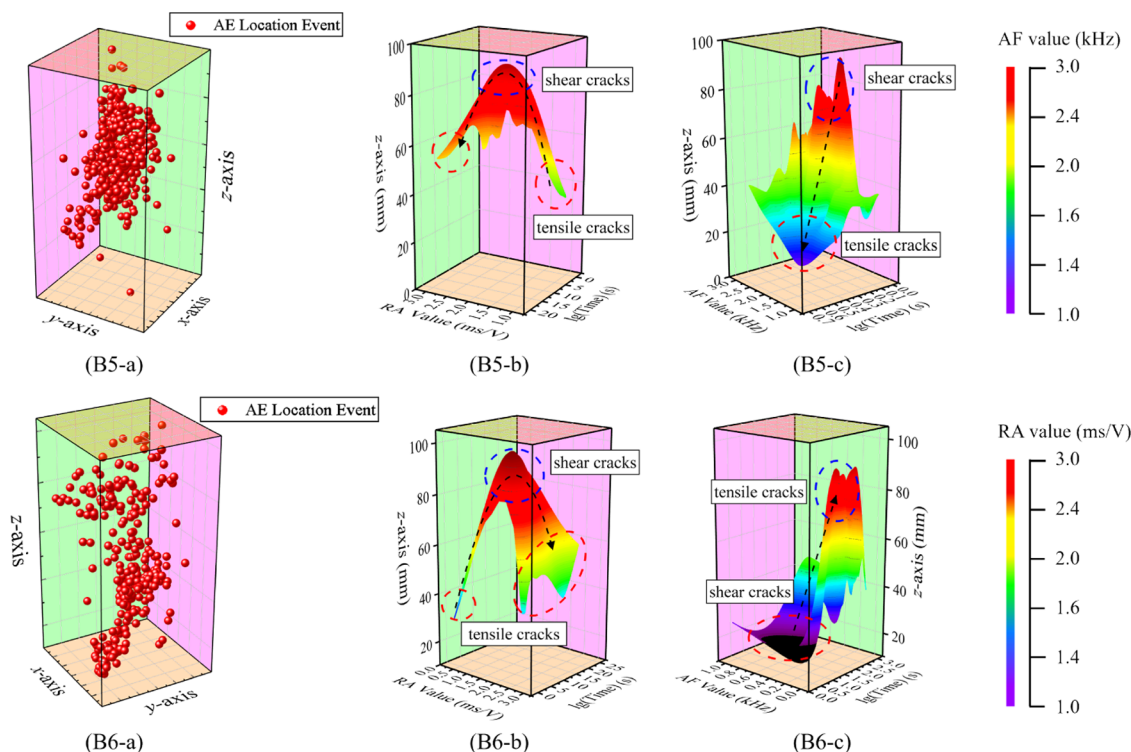

Figure 7. Location of AE events and spatial−temporal distribution of fracture types in red sandstone: (B5-a) AE location events of specimen B5, (B5-b) spatial−temporal distribution of RA values of specimen B5, (B5-c) spatial−temporal distribution of AF values of specimen B5, (B6-a) AE location events of specimen B6, (B6-b) spatial−temporal distribution of RA values of specimen B6, and (B6-c) spatial−temporal distribution of AF values of specimen B6.

$10^4/s$) at elastic deformation stage under compression. For specimen B5, AE ring counts were generally with low values and its value was no more than $10^4/s$, and for specimen B6, the value of AE ring counts was no more than $25 \times 10^3/s$. This indicated that there were fewer microcracks inside rocks at the elastic deformation stage, and rocks had not undergone severe damage, the rock specimen was at relatively stable state. However, when the compression stress reached the elastic limit stress, the internal fracture exploded, and the value of AE ring counts surged to a high level. For specimens B5 and B6, its value was

more than $1.75 \times 10^5/s$. Compared with the above-mentioned sudden increase of AE ring counts, the value of AE ring counts briefly fluctuated before peak stress, and this period was termed as the "relatively quiet period". The brittle fracture process of rocks was occurred at the "relatively quiet period", which can be considered as a typical precursor of rock failure.

It is crucial for distinguishing tensile and shear cracks of rocks by the relative values of RA and AF value. Both the relatively large values of RA value and the relatively small values of AF value mean the shear cracks inside rocks. Similarly, both the
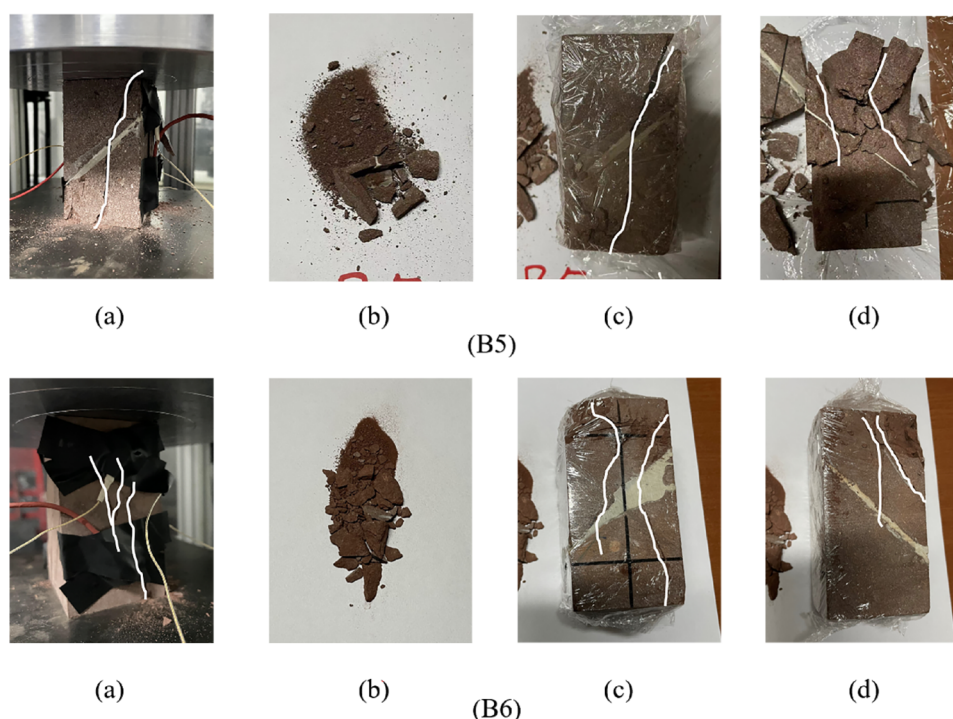
Figure 8. Macroscopic failure characteristics of rock specimens under compression: (B5-a, b, c, and d) macroscopic failure situations of specimen B5 and (B6-a, b, c, and d) macroscopic failure situations of specimen B6.

relatively small values of RA value and the relatively large values of AF value mean the tensile cracks inside rocks. Generally, the tensile and shear cracks can be distinguished based on a straight line with a slope of 1 passing through the origin point at the RA−AF diagrams.[26−30] In the previous studies,[26−30] the tensile cracks and shear/mixed-mode cracks were distinguished by the above mentioned method, as shown in Figure 6 (line 0: the sloping blue dotted line). In this study, to accurately distinguish the types of failure cracks,[26−30] the RA−AF diagram was further divided into three failure regions, namely, regions (I), (II), and (III), as shown in Figure 6. Regions (I), (II), and (III) represent the tensile, mixed tension−shear, and shear failure cracks, respectively. This classification method followed the above-mentioned classification principles,[26−30] and according to the distribution of AF and RA values, RA = 0.3 and AF = 0.3 was selected as the boundary for classification. The results revealed that this method can accurately characterize the actual microscopic failure types of rocks.

Then, this study further analyzed the spatio-temporal evolution characteristics of tensile and shear cracks of rocks, as shown in Figure 7. In Figure 7, the x-axis represents the compression time, the y-axis represents the AF values in Figure 7 (B5-b) and Figure 7 (B6-b), and the y-axis represents the RA values in Figure 7 (B5-c) and Figure 7 (B6-c), and the z-axis represents the Z coordinate of AE localization events. Then, this figure reveals the evolution pattern, in the Z direction of specimens, of AF or RA values with the increase of time. As a matter of fact, the AE localization events can determine the location information of rupture source inside rocks, but it cannot distinguish the rupture types of rock failure. Actually, each AE event of specimens corresponds to an occurrence time t_i, and each tensile or shear failure cracks also corresponds to an occurrence time t_i, which characterized by AE parameters. Subsequently, the Z coordinate of AE location events was further extracted. Then, the compression time t_i was used as the

link to combine the information of AE location events and the rupture types of specimens Figure 7. Figure 7 reveals the evolution trend of fracture types in Z direction of rocks. Notably, to enhance the readability of three-dimensional visualization of different rupture types, the logarithm base 10 was taken for the time, which made the entire drawing area relatively in agreement. As shown in Figure 7 (B5-b), for specimen B5, the RA value increased first and then decreased with the increase of time. Overall, its larger value, more than 1.75, was essentially in the upper space of the specimen. It demonstrated that the tensile failure cracks mainly occurred in the upper part of specimen B5. It meant that the fracture, inside specimen B5, gradually developed from shear fracture to tensile fracture (on the upper part of specimen B5) and then grew into shear fractures. Then, as shown in Figure 7 (B5-c), for specimen B5, the AF value was larger, more than 1.5, at the beginning of rock deformation. It demonstrated that tensile failure cracks first occurred in the upper space of the specimen. For specimen B5, it can be seen that RA value, in Figure 7 (B5-b), was relatively smaller, less than 1.5, while AF value, in Figure 7 (B5-c), was locally smaller, less than 2.0, at the same deformation stage. Therefore, the mixed tensile and shear failure cracks mainly occurred in the middle position of specimen B5. For specimen B6, the fracture types can be clearly distinguished and described through three-dimensional visualization in Figure 7 (B6-b) and (B6-c). Similarly, RA values of specimen B6 started at a low level, less than 1.0, then jumped to a high level, more than 1.5, and finally declined, as shown in Figure 7 (B6-b). Obviously, the tensile failure cracks mainly occurred at the top part of specimen B6, and the mixed tensile−shear failure cracks mainly occurred at the early and later deformation stage. As shown in Figure 7 (B6-c) (for specimen B6), at the initial deformation stage of rocks, AF value was relatively smaller, less than 0.6, which indicated that shear failure cracks mainly occurred at the bottom of specimen B6. Subsequently, at the later deformation stage, AF value of
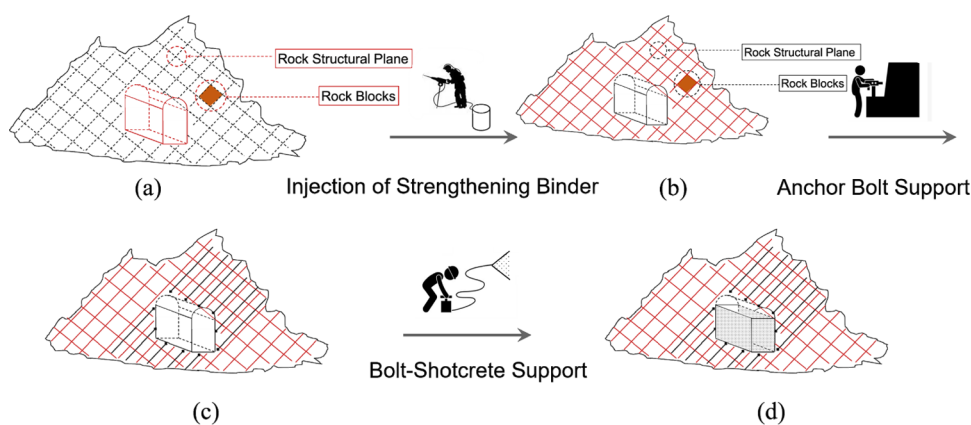
Figure 9. Schematic diagram of rock mass stability control measures with weak discontinuities: (a) rock mass with fractured structural surfaces, (b) rock mass after injection of strengthening binder, (c) rock mass after anchor bolt support, and (d) rock mass after bolt−shotcrete support.

specimen B6 jump increased, and it indicated that the mixed tensile−shear failure cracks mainly occurred at the upper edge of specimen B6.

4.2. Macroscopic Failure Characteristics of Rocks with Strongly Cemented Discontinuities. By monitoring the failure process of rocks, it can be seen that red sandstone mainly underwent elastic−brittle failure under uniaxial compression. After short compaction deformation, the specimens entered a stable elastic deformation stage without obvious crack propagation on the surface of rocks. Additionally, it was observed that shear and tensile cracks still did not appear on the surface of rocks at the peak stress. Instead, the specimens produced a "bang" sound after the stress slightly decreased, and the macroscopic cracks extended to the surface of specimens. Therefore, for rocks with strongly cemented discontinuities, the initiation of cracks occurred inside specimens first and gradually spread outward to the surface. Additionally, most cracks were shear and split cracks in the vertical direction of specimens. The cracks ran through the specimens on both sides of the strongly cemented structural plane, but few cracks ran vertically through the cemented structural plane.

Accordingly, the strong cohesive effect can reduce the failure tendency, fail from the potential slip fracture plane, of rocks, and it also reduced the development of large-scale shear cracks. The cemented discontinuities also prevented the propagation of fracture initiating from potential soft discontinuities, and it also affected the occurrence location of macroscopic fracture discontinuities. A preset structural plane will lead to the development of shear fracture of rocks. However, owing to the strong bonding effect, it was difficult for shear cracks to expand along the structural plane, and only some shear cracks and tensile cracks formed at a smaller scale and further coalesced with the main shear fracture.

5. DISCUSSIONS

5.1. Influence of a Strong Cement Structure on Failure Modes of Rock Specimens. Owing to the presence of structural planes, the rocks underwent substantial frictional damage under continuous compression, and the fragmentation of rocks was relatively scattered. The fragment size ranged from debris to broken blocks, and the shear strength of rocks generally decreased. As shown in Figure 8, the failure specimens were mainly debris and small fragmentation. Therefore, the strongly cemented discontinuities influenced the failure modes of rocks with discontinuities. Therefore, macroscopic failure did not

initiate from the discontinuities, and it started from the interior of rocks. The strongly cemented discontinuities enhanced the shear strength and the stability of rock discontinuities. Moreover, compared with Figure 7 (B5-a), its AE localization events were mainly concentrated in the upper area of specimen B5, which indicated that the main fracture behavior mainly occurred in the upper region of specimen B5, and the actual damage situation also verified this result, as shown in Figure 8 (B5-d). For specimen B6, its AE localization events were irregularly distributed up and down in the specimen. Therefore, the failure cracks of specimen B6 were also distributed up and down in specimen B6, as shown in Figure 8 (B6-c) and (B6-d).

Figure 7 shows that tensile failure cracks mainly occurred in the upper areas of rocks, while shear failure cracks mainly occurred at the bottom part of rocks. In other words, the strongly cemented discontinuities affected the failure modes of upper and lower rock blocks. The rough undulations of most structural planes in natural rocks are irregular. It is well known that when rock mass shears along the structural plane, the shear resistance of fracture surface is determined by the friction of rock blocks.[32] In this study, the rock structural plane was strengthened by solid gum. Thus, the fracture between rock structural planes was greatly reduced. Fault-slip rockbursts primarily occur in the sidewall or roof of a tunnel, the locations are exposed by excavation, and the structural plane is characterized by high shear strength, tight inclusion, and no filling.[6] The probability of encountering rockburst is lower with an unexposed structural plane.[9] Obviously, increasing the strength of discontinuities is an effective measure for enhancing the stability of rocks with discontinuities. However, a few specimens were tested in this study, the effect of angle and thickness of the structural plate was not considered, and the tests were limited to the case that the strength of structural plate was higher than the strength of rocks. The effect of these issues will be addressed in the future work.

5.2. Suggestions for Support and Stability Control of Weak Broken Rock Mass. Owing to the strongly cemented structural planes, the rock specimen no longer slides along the potential sliding fracture plane. Moreover, strong cementation enhances the bond strength of original weak structural plane and converts the weak structural plane into a strong structural plane. The strong structural planes are connected, inside the rocks, to form regional strengthening zones, as shown in Figure 9. The strengthened zones are similar to the reinforced skeleton in the

building structure, and the shear strength of rocks is enhanced, which can improve the stability of rock mass.

For rocks with abundant joints, more internal structural planes lead to poor stability and low strength. Under this condition, the effective support and stability control measures are implemented directly, which affects the stability of engineering structures and the safety of workers. For rock mass with elastic−brittle characteristics and abundant joint surfaces, it is better to form supporting structures and strengthening surfaces with high strength and strong cohesive force inside rocks, which is the first and key step for stability control of rocks. The supporting effect of subsequent conventional support measures is directly affected by the reinforcement zone of high-strength structures, which formed inside rocks. If the supporting structure or bonding surface cannot be formed inside rock mass, any subsequent bolt and shotcrete support will fail to guarantee a strong stable structure and strong shear strength body (surface). As shown in Figure 9a,b, first, the strong binder was injected into the broken joint surface by high-pressure equipment, and then, a strengthened area with larger shear strength initially formed inside rock mass. Subsequently, according to the support strength requirement, the rock mass was supported by the conventional bolt and shotcrete, which can further enhance the stability of rocks and ensure the structural stability and safety of engineering rock mass.

6. CONCLUSIONS

Based on AE monitoring experiment of red sandstone under uniaxial compression, the spatial−temporal failure characteristics of rocks with cemented structural planes were analyzed and the following conclusions were obtained.

(1) A strong cemented structural plane was added to red sandstone, and the spatial−temporal failure characteristics of specimens were clearly analyzed. A shear failure mechanical model of rock discontinuities revealed that the strongly cemented discontinuities can enhance the shear strength of rocks.

(2) The microscopic failure evolution characteristics of rocks with a strongly cemented structural plane were obtained under uniaxial compression. The results revealed that AE ring counts were generally increased in the "quiet period" at the elastic deformation stage. Then, in the brittle failure stage, AE ring counts initially exhibited an obvious jump increase phenomenon and then it entered a "relatively quiet period", which was regarded as a typical precursor of the forthcoming failure of rocks.

(3) The spatial−temporal evolution characteristics of internal fracture of rocks were investigated under uniaxial compression. The results demonstrated that the internal fracture locations were scattered at the initial deformation stage. Subsequently, the rock fracture positions diverged and the fracture developed to mixed tensile−shear cracks. The failure types of rock specimens were also further distinguished in detail.

■ AUTHOR INFORMATION

Corresponding Authors

Ansen Gao − School of Mechanics and Civil Engineering, China University of Mining & Technology (Beijing), Beijing 100083, People's Republic of China; Email: gaoansen@student.cumtb.edu.cn

Chengzhi Qi − School of Mechanics and Civil Engineering, China University of Mining & Technology (Beijing), Beijing 100083, People's Republic of China; School of Civil and Transportation Engineering and Beijing Advanced Innovation Centre for Future Urban Design, Beijing University of Civil Engineering and Architecture, Beijing 100044, People's Republic of China; orcid.org/0000-0001-6976-9369; Email: buceaqcz@163.com

Authors

Renliang Shan − School of Mechanics and Civil Engineering, China University of Mining & Technology (Beijing), Beijing 100083, People's Republic of China

Chunlai Wang − School of Energy and Mining Engineering, China University of Mining & Technology (Beijing), Beijing 100083, People's Republic of China

Complete contact information is available at:
https://pubs.acs.org/10.1021/acsomega.2c02169

■ ACKNOWLEDGMENTS

■ REFERENCES

(1) Feng, G. L.; Feng, X. T.; Chen, B. R.; Xiao, Y. X.; Yu, Y. A microseismic method for dynamic warning of rockburst development processes in tunnels. Rock Mech. Rock Eng. 2015, 48, 2061−2076.

(2) Keneti, A.; Sainsbury, B. A. Review of published rockburst events and their contributing factors. Eng. Geol. 2018, 246, 361−373.

(3) Ortlepp, W. D. Observation of mining-induced faults in an intact rock mass at depth. Int. J. Rock Mech. Min. Sci. 2000, 37, 423−436.

(4) Meng, F. Z.; Zhou, H.; Wang, Z. Q.; Zhang, L. M.; Kong, L.; Li, S. J.; Zhang, C. Q. Experimental study on the prediction of rockburst hazards induced by dynamic structural plane shearing in deeply buried hard rock tunnels. Int. J. Rock Mech. Min. Sci. 2016, 86, 210−223.

(5) Meng, F. Z.; Zhou, H.; Wang, Z. Q.; Zhang, L. M.; Kong, L.; Li, S. J.; Zhang, C. Q.; Hu, S. C. Experimental study of factors affecting fault slip rockbursts in deeply buried hard rock tunnels. Bull. Eng. Geol. Environ. 2017, 76, 1167−1182.

(6) Zhou, H.; Meng, F. Z.; Zhang, C. Q.; Hu, D. W.; Yang, F. J.; Lu, J. J. Analysis of rockburst mechanisms induced by structural planes in deep tunnels. Bull. Eng. Geol. Environ. 2015, 74, 1435−1451.

(7) Chen, X. J.; Li, L. Y.; Wang, L.; Qi, L. L. The current situation and prevention and control countermeasures for typical dynamic disasters in kilometer-deep mines in China. Saf. Sci. 2019, 115, 229−236.

(8) Feng, F.; Li, X. B.; Luo, L.; Zhao, X. D.; Chen, S. J.; Jiang, N.; Huang, W. P.; Wang, Y. J. Rockburst response in hard rock owing to excavation unloading of twin tunnels at great depth. Bull. Eng. Geol. Environ. 2021, 80, 7613−7631.

(9) Feng, F.; Li, X. B.; Rostami, J.; Li, D. Y. Modeling hard rock failure induced by structural planes around deep circular tunnels. Eng. Fract. Mech. 2019, 205, 152−174.

(10) Durrheim, R. J.; Roberts, M. K. C.; Haile, A. T.; Hagan, T. O.; Jager, A. J.; Handley, M. F.; Spottiswoode, S. M.; Ortlepp, W. D. Factors influencing the severity of rockburst damage in South African gold mines. J. South. Afr. Inst. Min. Metall. 1998, 98, 53−57.

(11) Ortlepp, W. D.; Stacey, T. R. Rockburst mechanisms in tunnels and shafts. *Tunnelling Underground Space Technol.* **1994**, *9*, 59−65.

(12) Feng, G. L.; Feng, X. T.; Chen, B. R.; Xiao, Y. X.; Zhao, Z. N. Effects of structural planes on the microseismicity associated with rockburst development processes in deep tunnels of the Jinping-II Hydropower Station, China. *Tunnelling Underground Space Technol.* **2019**, *84*, 273−280.

(13) Hu, L.; Feng, X. T.; Xiao, Y. X.; Wang, R.; Feng, G. L.; Yao, Z. B.; Niu, W. J.; Zhang, W. Effects of structural planes on rockburst position with respect to tunnel cross-sections: a case study involving a railway tunnel in China. *Bull. Eng. Geol. Environ.* **2020**, *79*, 1061−1081.

(14) Song, D. Q.; Chen, J. D.; Cai, J. H. Deformation monitoring of rock slope with weak bedding structural plane subject to tunnel excavation. *Arabian J. Geosci.* **2018**, *11*, 1−10.

(15) Ma, D.; Kong, S. B.; Li, Z. H.; Zhang, Q.; Wang, Z. H.; Zhou, Z. L. Effect of wetting-drying cycle on hydraulic and mechanical properties of cemented paste backfill of the recycled solid wastes. *Chemosphere* **2021**, *282*, No. 131163.

(16) Lu, Y. L.; Wang, L. G.; Li, Z. L.; Sun, H. Y. Experimental Study on the Shear Behavior of Regular Sandstone Joints Filled with Cement Grout. *Rock Mech. Rock Eng.* **2017**, *50*, 1321−1336.

(17) Sun, S. R.; Sun, H. Y.; Wang, Y. J.; Wei, J. H.; Liu, J.; Kanungo, D. P. Effect of the combination characteristics of rock structural plane on the stability of a rock-mass slope. *Bull. Eng. Geol. Environ.* **2014**, *73*, 987−995.

(18) Zong, Y. J.; Han, L. J.; Han, G. L. Study on shear properties of rock structural plane by grouting reinforcement. *Adv. Mater. Res.* **2011**, *250−253*, 1520−1526.

(19) Ma, D.; Duan, H.; Zhang, Q.; Zhang, J. X.; Li, W. X.; Zhou, Z. L.; Liu, W. T. A numerical gas fracturing model of coupled thermal, flowing and mechanical effects. *Comput. Mater. Continua* **2020**, *65*, 2123−2141.

(20) Ma, D.; Duan, H. Y.; Liu, W. T.; Ma, X. T.; Tao, M. Water-sediment two-phase flow inrush hazard in rock fractures of overburden strata during coal mining. *Mine Water Environ.* **2020**, *39*, 308−319.

(21) Shan, R. L.; Bai, Y.; Ju, Y.; Han, T. Y.; Dou, H. Y.; Li, Z. L. Study on the triaxial unloading creep mechanical properties and damage constitutive model of red sandstone containing a single ice-filled flaw. *Rock Mech. Rock Eng.* **2021**, *54*, 833−855.

(22) Kong, X. S.; Xu, Z. Z.; Shan, R. L.; Liu, S.; Xiao, S. C. Investigation on groove depth of artificial dam of underground reservoir in coal mines. *Environ. Earth Sci.* **2021**, *80*, No. 214.

(23) Hoek, E.; Brown, E. T. Empirical strength criterion for rock masses. *J. Geotech. Eng.* **1980**, *106*, 1013−1035.

(24) Hoek, E.; Brown, E. T. The Hoek-Brown failure criterion and GSI-2018 edition. *J. Rock Mech. Geotech. Eng.* **2019**, *11*, 445−463.

(25) Labuz, J. F.; Zang, A. Mohr-Coulomb failure criterion. *Rock Mech. Rock Eng.* **2012**, *45*, 975−979.

(26) Aggelis, D. G. Classification of cracking mode in concrete by acoustic emission parameters. *Mech. Res. Commun.* **2011**, *38*, 153−157.

(27) ElBatanouny, M. K.; Larosche, A.; Mazzoleni, P.; Ziehl, P.; Matta, F.; Zappa, E. Identification of cracking mechanisms in scaled FRP reinforced concrete beams using acoustic emission. *Exp. Mech.* **2014**, *54*, 69−82.

(28) Elfergani, H. A.; Pullin, R.; Holford, K. M. Damage assessment of corrosion in prestressed concrete by acoustic emission. *Constr. Build. Mater.* **2013**, *40*, 925−933.

(29) Rodríguez, P.; Celestino, T. B. Application of acoustic emission monitoring and signal analysis to the qualitative and quantitative characterization of the fracturing process in rocks. *Eng. Fract. Mech.* **2019**, *210*, 54−69.

(30) Du, K.; Li, X. F.; Tao, M.; Wang, S. F. Experimental study on acoustic emission (AE) characteristics and crack classification during rock fracture in several basic lab tests. *Int. J. Rock Mech. Min. Sci.* **2020**, *133*, No. 104411.

(31) Christian, U. G.; Masayasu, O.; Dimitrios, G. A.; Tomoki, S. *Acoustic Emission Testing: Basics for Research-Applications in Engineering*, 2nd ed.; Springer Nature Switzerland AG: Gewerbestrasse 11, 6330 Cham, Switzerland, 2021; pp 117−171.

(32) Dong, S.; Feng, W. K.; Yin, Y. B.; Hu, R.; Dai, H. C.; Zhang, G. Q. Calculating the permanent displacement of a rock slope based on the shear characteristics of a structural plane under cyclic loading. *Rock Mech. Rock Eng.* **2020**, *53*, 4583−4598.